Stability and rocking response of non-uniform masonry arches: The 'part-elliptical' profile

Aikaterini Leontari [a],[*], Marios Apostolou [b]

[a] School of Civil Engineering, National Technical University, Athens, Greece
[b] Department of Architectural Engineering, University of Ioannina, Ioannina, Greece

ABSTRACT

The fundamental role of geometry on the stability of historical arched structures has been unveiled centuries ago. In this study, a segmental arch consisting of an elliptical upper part (extrados) and a circular lower part (intrados) is introduced. This so-called part-elliptical arch is treated as a rigid monolithic body enabled to rock on a triggering base. The objective of the study is to extend the established methods applicable to the conventional circular arches, particularly in terms of: (i) stability analysis at incipient uplift, (ii) time-history analysis of the rocking response. The results are presented comparatively to those extracted from the circular arch of the same geometric characteristics.

1. Introduction – Description of work

Stability of masonry arches has always been a challenging task for architects and builders over the centuries. Nevertheless, the scientific community has started to be intrigued by this subject merely at the eighteenth century. Couplet, in his 1729′s pioneering work [1], was the first to successfully demonstrate the way a semi-circular arched structure can safely withstand its gravity load, in the framework of a structural mechanics approach. He unveiled the purely geometrical nature of the problem in a sense that collapse is not associated with material crushing but it involves the mobilisation of a kinematic mechanism. Accordingly, a graphical approach can be introduced to determine potential equilibrium or collapse mechanisms through the notion of the thrust line. Equilibrium is established when the thrust line lies inside the arch, whereas collapse occurs as soon as the thrust line intersects the external curves. Couplet calculated the minimum required slenderness, t/R, of the semi-circular arch so that the thrust line be marginally bounded by the outer lines of the arch and limit equilibrium be established. This assumption was based on a failure mechanism through the formation of four hinges but Couplet erroneously predefined the intrados hinges at an angle of 45° with respect to the spring points. Milankovitch [2], motivated by Couplet's innovative work revisited the theory of thrust line and computed the exact location of the intrados hinge at 54.5°, thus correcting the minimum required slenderness, t/R, from 0.101 to 0.1075. In recent years, Alexakis & Makris [3,4]

investigated thoroughly the stability of a monolithic segmental arch setting the embrace angle, β, as a parameter of the design. They demonstrated that in a continuous arch the hinge locations should not be predefined but they had to be computed. In this way, they introduced a variational formulation incorporated in the principle of stationary potential energy to derive the minimum thickness slenderness, t/R, for different values of β. The results demonstrate the favourable role of base confinement, as the minimum required slenderness, t/R, gradually reduces from 0.1075 at the semi-circular arch ($\beta = \pi$) down to 0.0075 at the segmental circular arch of $\beta = \pi/2$. Inherent to the aforediscussed analytical studies are the so-called Couplet-Heyman postulates, considering for the masonry infinite compressive strength, zero tensile strength, and the coefficient of friction large enough to prevent sliding [5].

Unlike the stability of the masonry arch under self-weight, the response due to lateral dynamic loads didn't receive much attention until Oppenheim's notable work, merely in 1992 [6]. He derived the nonlinear equation of motion of a segmental circular arch consisting of seven voussoirs which together with the supporting base form eight radial joints. Since the arch is not considered as a monolithic structure, the imminent hinges can occur only at these predefined physical joints. Upon the application of rectangular pulses as input base motion, the arch was converted into a four-link mechanism of fixed hinge locations. This procedure allowed for the computation of the arch motion before the first impact occurs. Within the framework of time-history dynamic

analysis it is critical to determine the criterion for the phase transition from the full contact to rocking regime. Stability analysis in static terms can be used to this respect, on the condition of incipient uplift. Clemente [7] adopted an iterative procedure based on an energy approach to derive minimum levels of ground acceleration, as well as to calculate the hinge locations at the onset of rocking mode, for different values of the slenderness, t/R, and the angle of embrace, β. Ochsendorf [8], based on Clemente's concept, proposed an alternative iterative procedure for stability analysis under constant horizontal acceleration. A growing interest in the stability assessment of masonry arches using the limit analysis theory has lately been emerged in literature [9–14]. Recent studies further contributed to the arch seismic response under pulse-type ground motion, based either to analytical or to numerical methods [15–20]. In the latter, primarily the finite element method (FEM) as well as the discrete element method (DEM) are involved. A thorough comparative study on these methods has been presented by Sarhosis et al [21]. Many researchers have extensively implemented the DEM [9,21,22–24] to assess the collapse behaviour of masonry arches.

While masonry arches of a uniform circular and sometimes elliptical profile have been subjected to thorough scrutiny in the past, only a few studies have addressed the non-uniform arch [9,12,25]. As an exception, Milankovitch in his doctoral dissertation developed the theory of the thrust line with reference to a masonry arch of variable thickness [2]. In the general case, the intrados and extrados lines are determined by two generic continuous functions so that the variable thickness of the arch

ring can be considered. Despite the lack of theoretical background, the non-uniform arch has been implemented in the design of numerous historical bridges around the world. D′ Agostino & Bellomo document that historical bridges of a large span have a gradually increasing thickness from the key to the springers at a ratio of 1.1–1.6 [26]. Two representative examples of such stone bridges are portrayed in Fig. 1.

Prompted by the lack of detailed investigation, the present study is oriented to non-uniform arches with the following geometrical particularity: elliptical at the extrados (upper curve) yet circular at the intrados (lower curve). For simplicity, this profile will be referred from now on as *a part-elliptical*. The objective is to investigate the role of the extrados curve on the structural performance of the arch under base horizontal motion.

In light of the above, the analysis of rocking response is divided in two steps [3,6]: (a) stability analysis is performed in static terms to calculate the hinge locations as well as the minimum ground acceleration at the onset of rocking, given the slenderness and the angle of embrace of the arch (t/R, β), (b) time-history analysis of rocking prior to impact is then feasible as the transition criterion from the full-contact to rocking phase has been established from the previous step. Regarding the first step, a rigorous variational formulation is implemented by adopting the principle of minimum total potential energy, $P = U + V$, where U is the elastic strain energy and V is the potential energy associated with force of gravity. According to this principle, the total energy is at a stationary position when an infinitesimal variation from

a.
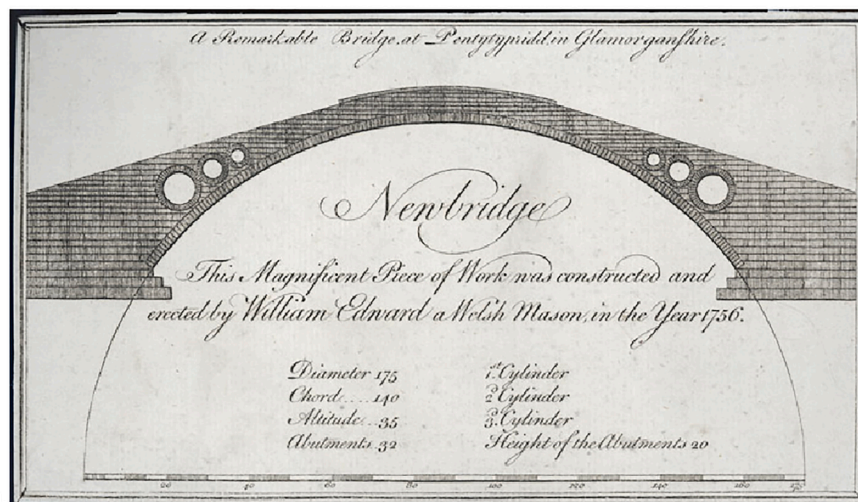
b.

Fig. 1. Two typical part-elliptical bridges: (a) Templas bridge, Aetolia-Akarnania, Greece. (b) The Bridge at Pontypridd, Wales.

such position involves no change in energy meaning that $\delta P = 0$. As no elastic deformation is considered ($U = 0$), it eventually yields that $\delta V = 0$. The second step deals with the time-history analysis of rocking response with analytical or numerical methods. Similar to the circular case, rocking of the arch ring is associated with a one-degree-of-freedom vibration once a four-link kinematic mechanism is developed. In the analytical procedures, the equation of motion derived with Lagrangian formulation is employed. Whenever a closed-form solution of equation of motion is not tractable the software system "Mathematica" is utilised to extract the analytical solution. For the purposes of the numerical procedures, a two-dimensional finite element modelling is implemented. Numerical results are then discussed and compared to those provided by the analytical method. A comprehensive approach to gain insight to the geometrically nonlinear response of part-elliptical arches in the time-domain is through idealised pulses. Simple pulses are employed in the analysis not just to represent near-fault ground motion but also because in many cases the time history of the recorded acceleration can effectively be trimmed to a one-cycle pulse.

Prior to the analysis of the part-elliptical profile the study revisits the uniform circular arch in Section 2, in terms of calculation of the imminent hinges. Hence, the afore-described principle of minimum potential energy is engaged to extract closed-form solution of the hinge locations whereas the results are presented comparatively to those of the semi-analytical approach [3]. In Section 3, the response of the part-elliptical arch subjected to a horizontal acceleration is investigated. In particular, the model parameters are described in Section 3.1. Stability analysis is then presented in static terms in Section 3.2 through variational and Lagrangian formulation (Sections 3.2.1 and 3.2.2 respectively). In Section 3.3, a time-history analysis of the response is performed through analytical and finite element approaches (described in Sections 3.3.1 and 3.3.2 respectively). To this end the results of a comparative study are presented in Section 3.3.3. The performance of the part-elliptical arch is evaluated with reference to the uniform, circular arch. Moreover, the two methods of analysis are also compared in the same section, in terms of time-histories of the problem parameters.

It is worthy of note that this study regards only the weight of the arch ring. This simplification allows to isolate the response of the arch itself excluding the effect (beneficial or detrimental) of additional dead loads of spandrels, backfills etc. Moreover, it enables comparison of the results with some well-established studies of the literature. An extension of the analytical and numerical model that will simulate realistic conditions comprising of more complex loads and boundaries is worth contemplating in future work.

2. Revisiting the circular arch

2.1. Calculation of hinge locations in previous studies

As stone is a material strong enough to crush under compression, the only failure mode of a masonry arch is through the formation of no-tension hinges that turns the structure into a rocking mechanism. In dynamic terms, as soon as the critical uplift acceleration is reached, a stone arch of mid-thickness radius R, thickness t, and of angle-of-embrace β, becomes a four-hinge mechanism and the blocks rock one to the other as portrayed in Fig. 2 (left side). It is implied that the structural stiffness is large enough so that in the full-contact phase no flexural displacements are developed. Evidently, in this regime the arch performs as a rigid body that follows the ground motion.

The question arising is to locate the points of rupture under a specific horizontal acceleration. A first approach was to consider that hinges develop at the physical joints of the blocks [6]. In a subsequent approach the circular stone arch was treated as monolithic and the imminent hinges were determined by a method based on a variational formulation and the application of the principle of stationary potential energy [3]. This procedure is presented briefly and emphasis is given to the proposed analytical solution. In Fig. 2 (left side) the location of the four hinges of the rocking mechanism developed by horizontal acceleration $\ddot{x}_g = \varepsilon g$ is depicted in which ε is the seismic coefficient, and g is the acceleration of gravity. In this work, a two-springing collapse mechanism is studied which means that hinges A and D form at the extrados right springing (position φ_0) and the intrados left springing (position φ_3) respectively. On the other hand, hinges B and C form at the main arch body at positions φ_1 and φ_2 respectively. The weights (W_i) and the co-ordinates of the centre of gravity (x_i, y_i) of segment 2 (segment BC), segment 3 (segment CD) and the combined segment 1–2 (segment ABC) are presented in Eqs. (1) and (2). The limit equilibrium state of each segment (2,3, 1–2) is described below through Eqs. (3) and (4). The internal thrust force at point C (T_c) is analysed to the unknown horizontal and vertical components (T_{cx}), (T_{cy}) respectively (Fig. 2 right).

For segments 2 and 3 (BC and CD respectively) it yields:

$$W_i = \rho g 2R^2 r'(\varphi_i - \varphi_{i-1})$$

$$x_i = R\left(1 + \frac{r'^2}{3}\right)\frac{\sin\varphi_i - \sin\varphi_{(i-1)}}{\varphi_i - \varphi_{(i-1)}}, y_i = -R\left(1 + \frac{r'^2}{3}\right)\frac{\cos\varphi_i - \cos\varphi_{(i-1)}}{\varphi_i - \varphi_{(i-1)}}$$

$$(1)$$

where i = 2 or 3, and $r' = \frac{t}{2R}$. Likewise, for the combined segment 1–2 (ABC) it yields:

$$W_{(i-1)-i} = \rho g 2R^2 r'\left(\varphi_i - \varphi_{(i-2)}\right)$$

$$x_{(i-1)-i} = R\left(1 + \frac{r'^2}{3}\right)\frac{\sin\varphi_i - \sin\varphi_{(i-2)}}{\varphi_i - \varphi_{(i-2)}}, y_{(i-1)-i}$$

$$= -R\left(1 + \frac{r'^2}{3}\right)\frac{\cos\varphi_i - \cos\varphi_{(i-2)}}{\varphi_i - \varphi_{(i-2)}}$$

$$(2)$$

where i = 2, and $r' = \frac{t}{2R}$. In both sets of Eqs. (1) and (2), density ρ is considered constant.
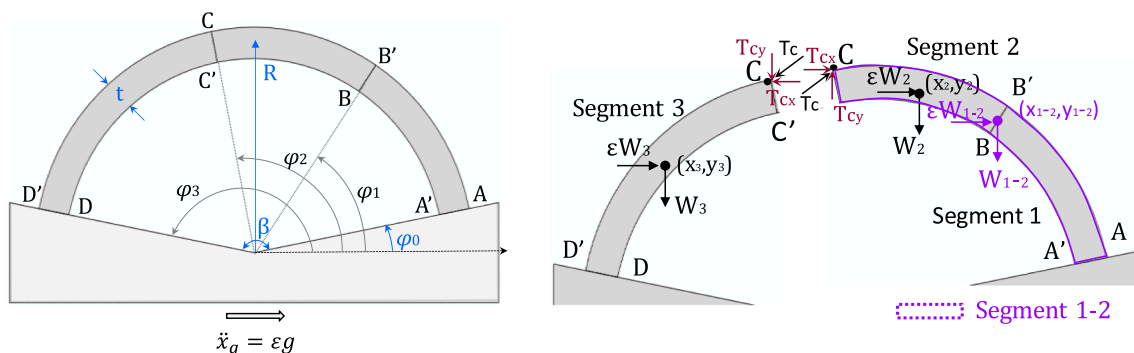

Fig. 2. The circular arch with mid-thickness radius R, thickness t and angle of embrace β becomes a four-hinge mechanism when subjected to horizontal ground acceleration $\ddot{x}_g = \varepsilon g$ (left). Limit equilibrium analysis applied to the arch (right).

Moment equilibrium of segments 2, 3 about hinge B and C respectively, in a slightly different formulation to that developed in [3] yields:

$$a_i T_{c_x} + b_i T_{c_y} + f_i = 0$$

$$a_i = R((r' \pm 1)sin\varphi_i - (1 \mp r')sin\varphi_{(i-1)})$$

$$b_i = R((1 \mp r')cos\varphi_{(i-1)} - (1 \pm r')cos\varphi_i)$$

$$f_i = \frac{2r'R^3}{3cos\xi}((r'^2 + 3)(sin(\xi - \varphi_{(i-1)}) - sin(\xi - \varphi_i))$$

$$+ 3(r' - 1)(\varphi_i - \varphi_{(i-1)})cos(\xi - \varphi_*)) \quad (3)$$

where i = 2 or 3, $\varphi_* = \varphi_{(i-1)}$ for segment 2 and $\varphi_* = \varphi_i$ for segment 3. Likewise, moment equilibrium of the combined segment 1–2 about hinge A yields:

$$a_{(i-1)-i} T_{c_x} + b_{(i-1)-i} T_{c_y} + g f_{(i-1)-i} = 0$$
$$a_{(i-1)-i} = (r' + 1)R(sin\varphi_i - sin\varphi_{(i-2)})$$
$$b_{(i-1)-i} = (r' + 1)R(cos\varphi_{(i-2)} - cos\varphi_2)$$
$$f_{(i-1)-i} = \varepsilon W_{(i-1)-i}(y_{(i-1)-i} - (r' + 1)Rsin\varphi_{(i-2)}) + W_{(i-1)-i}(x_{(i-1)-i}$$
$$- (r' + 1)Rcos\varphi_{(i-2)}) \quad (4)$$

where the multiplier of the horizontal earthquake $\varepsilon = tan\xi$ and i = 2. By solving the above Eqs. (3), (4) it yields:

$$T_{c_x} = \frac{b_2 f_3 - b_3 f_2}{a_2 b_3 - b_2 a_3} \text{ and } T_{c_y} = \frac{a_3 f_2 - a_2 f_3}{a_2 b_3 - b_2 a_3} \quad (5)$$

$$(a_{(1-2)}b_2 - b_{(1-2)}a_2)f_3 + (b_{(1-2)}a_3 - a_{(1-2)}b_3)f_2 + (a_2 b_3 - b_2 a_3)f_{(1-2)} = 0 \quad (6)$$

The horizontal (T_{c_x}) and the vertical (T_{c_y}) components of the internal thrust force T_c are unfolded on Eq. (5). Moreover, Eq. (6) involves only the radius R, the slenderness r' and the angles φ_i (i = 1,2,3). Some of the formulae presented above (Eqs. (1)–(4)) can also be found in literature [3,4] however they are also included herein to facilitate independent reading.

2.2. Analytical calculation of hinge locations

Alternatively to what presented so far in literature [3,4], the left-hand side of Eq.(6) can be defined as a new function G of the independent variables r', R, φ_i, ξ, which should be zero: $G(R, r', \varphi_1, \varphi_2, \varphi_3, \xi) = 0$. The fourth power of the radius R is an overall factor, therefore, multiplying by the inverse R^{-4} a new function F independent of R is defined: $F(r', \varphi_1, \varphi_2, \varphi_3, \xi) = 0$, which can be written as a fourth-degree polynomial with respect to r':

$$F(r', \varphi_1, \varphi_2, \varphi_3, \xi) = \sum_{k=1}^{4} c_k r'^k = c_4 r'^4 + c_3 r'^3 + c_2 r'^2 + c_1 r' + c_0 = 0 \quad (7)$$

The coefficients c_k are known functions of the angles. Therefore, the solution of Eq. (4) can be expressed in terms of the roots of the polynomial (Eq. (7)). It is noteworthy that the roots can be extracted analytically as functions of the angles φ_i. After algebraic manipulations, the coefficients of the fourth-degree polynomial (Eq.7) are presented on Eq. (8) presented below:

$$c_4 = \kappa, \ c_3 = \mu - \lambda, \ c_2 = 3\kappa + \nu, \ c_1 = -(3\lambda + \mu), \ c_0 = \nu \quad (8)$$

$$\frac{\kappa}{2} = sin(\varphi_1 - \varphi_3)(sin\xi - sin\varphi_2) + sin(\xi - \varphi_2)(sin\varphi_1 - sin\varphi_3) \quad (9)$$

$$\frac{\lambda}{2} = sin(\varphi_1 - \varphi_3)(sin\xi - sin\varphi_2) - sin(\xi - \varphi_2)(sin\varphi_1 - sin\varphi_3) \quad (10)$$

$$\frac{\mu}{12} = (\varphi_1 - \varphi_2)cos\varphi_1 cos\frac{\xi - \varphi_3}{2} cos\frac{\varphi_2 - \varphi_3}{2} sin\frac{\xi - \varphi_2}{2}$$
$$+ (\varphi_2 - \varphi_3)cos\varphi_3 cos\frac{\xi - \varphi_1}{2} cos\frac{\varphi_1 - \varphi_2}{2} sin\frac{\xi - \varphi_2}{2}$$
$$+ (\varphi_2 - \xi)cos\xi cos\frac{\varphi_1 - \varphi_2}{2} cos\frac{\varphi_2 - \varphi_3}{2} sin\frac{\varphi_1 - \varphi_3}{2} \quad (11)$$

$$\frac{\nu}{3} = [(\varphi_2$$
$$- \varphi_1)cos\varphi_1 + sin\varphi_1 - sin\varphi_2][sin(\xi - \varphi_2) + sin(\varphi_2 - \varphi_3) + sin(\varphi_3 - \xi)][(\xi$$
$$- \varphi_2)cos\xi - sin\xi + sin\varphi_2][sin(\varphi_1 - \varphi_2) + sin(\varphi_2 - \varphi_3) + sin(\varphi_3 - \varphi_1)] + [(\varphi_2$$
$$- \varphi_3)cos\varphi_3 - sin\varphi_2 + sin\varphi_3][sin(\xi - \varphi_1) + sin(\varphi_1 - \varphi_2) + sin(\varphi_2 - \xi)] \quad (12)$$

According to the principle of stationary potential energy, every system in stable static equilibrium should have its potential energy minimised and therefore its partial derivatives with respect to the angles φ_i should be set equal to zero. The potential energy and the partial derivatives are given by the following forms, Eqs. (13) and (14) respectively:

$$V(r') = 4\rho R^3 sin\frac{\beta}{2} r' \left(1 + \frac{r'^2}{3}\right) \quad (13)$$

$$\frac{\partial V}{\partial \varphi_i} = 4\rho R^3 sin\frac{\beta}{2} \left(1 + r'^2\right) \frac{\partial r'}{\partial \varphi_i} = 0, \ i = 1, 2, 3 \quad (14)$$

where

$$\frac{\partial r'}{\partial \varphi_i} = 0, \ i = 1, 2, 3 \quad (15)$$

The derivative of r' (Eq. (15)) can be extracted when differentiating Eq. (7):

$$\frac{\partial r'}{\partial \varphi_i} = -\frac{\sum_{k=1}^{4} c_k^{(i)} r'^k}{\sum_{k=1}^{4} k c_k r'^{k-1}} \text{ where } c_k^{(i)} = \frac{dc_k}{d\varphi_i}, \ i = 1, 2, 3 \quad (16)$$

where $c_k^{(i)}$ defined in Eq. (8), are computed in terms of the angles φ_i through Eqs. (9)–(12).

In this way, the location of the hinges can be determined by setting the numerator of the right-hand side of Eq. (16) equal to zero. Therefore, solution is sought where Eqs. (7) and (16) hold simultaneously. Denote that Eq. (16) provides the analytical solution of the polynomial function in contrast to the approach presented in [3] that was based on numerical procedures. A graphic illustration of the solution can yield the location of the hinges. In the diagram of Fig. 3, the results of the analytical solution are compared to those derived numerically by Alexakis & Makris. The comparison is based on matching the location of the imminent hinges φ_1 and φ_2 of a circular arch for various angles of embrace β ($\beta =$
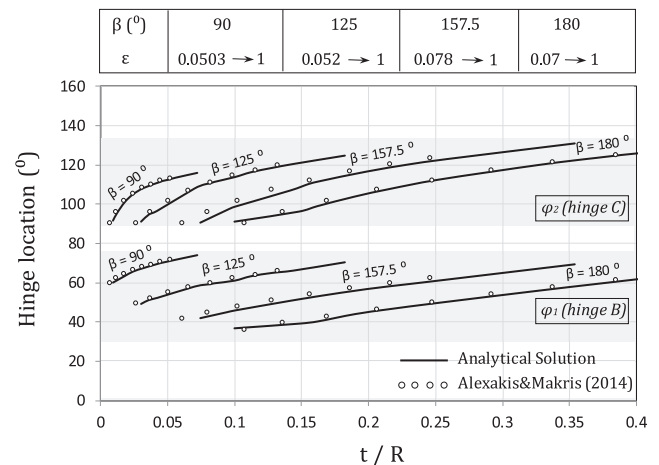
β (°)	90	125	157.5	180
ε	0.0503 → 1	0.052 → 1	0.078 → 1	0.07 → 1

Fig. 3. Location of the imminent hinges φ_1 and φ_2 at points B, and C respectively of a circular arch with a given angle of embrace β and slenderness t/R. Results of this work are compared with those obtained by Alexakis & Makris [3].

90°, 125°, 157.5°, 180°) and slenderness t/R. The range of seismic co-efficient ε associated with the curves is: $\varepsilon = 0.05$–1 for $\beta = 90°$, 125° and $\varepsilon = 0.07$–1 for $\beta = 157.5°$, 180°. The comparison is proved remarkably good indicating the accuracy of the proposed analytical solution. The slight difference observed in the case of $\beta = 157.5°$ is attributed to the comparison of the analytical solution with the other authors results of an arch of $\beta = 155°$.

3. Part-elliptical arch

3.1. Model parameters

Consider now the rigid masonry arch shown in Fig. 4 with the following particularity: circular on the inside (intrados) yet elliptical on the outside (extrados). In geometrical terms, this type of arch which from now on will be referred as part-elliptical, can be defined by the angle of embrace β, the thickness radius $R(\varphi)$, along with the shape parameters of the ellipse: the semi major and minor axes (a and b respectively, where $a > b > R(90°)$). In addition, as thickness t gradually decreases from the edge to the center, a nominal value has to be defined, which herein is set $t = t_{min}$ (i.e. the thickness at the mid-point axis). The aforementioned choice of the minimum value is considered more suitable not only for comparison purposes with arches of uniform thickness but also for computational simplicity as t in this position ($\varphi = 90°$) is independent of the angle of embrace β. The position of each focus of the ellipse is given in vector notation:

$$\overrightarrow{r}(\varphi) = \frac{ab}{\sqrt{b^2 cos^2\varphi + a^2 sin^2\varphi}} (i cos\varphi + j sin\varphi) \qquad (17)$$

in which, φ is the angle formed by the radius of the ellipse at a random point and the horizontal axis, whereas i and j represent the unit vectors with reference to the abscissa and the ordinate respectively. Accordingly, the thickness of the arch as a function of the angle, φ, is:

$$
x_2 = \frac{\left[-(r'-1)^3(sin\varphi_1 - sin\varphi_2) + \dfrac{(1+r')^3\left(-\dfrac{tan\varphi_1}{\sqrt{\lambda^2 + tan\varphi_1^2}} - \dfrac{tan\varphi_2}{\sqrt{\lambda^2 + tan\varphi_2^2}} \right)}{\lambda^2} \right]}{3W_2}
$$

$$
y_2 = \frac{\left[-(r'-1)^3(cos\varphi_1 - cos\varphi_2) + \dfrac{(1+r')^3\left(-\dfrac{1}{\sqrt{\lambda^2 + tan\varphi_1^2}} - \dfrac{1}{\sqrt{\lambda^2 + tan\varphi_2^2}} \right)}{\lambda} \right]}{3W_2}
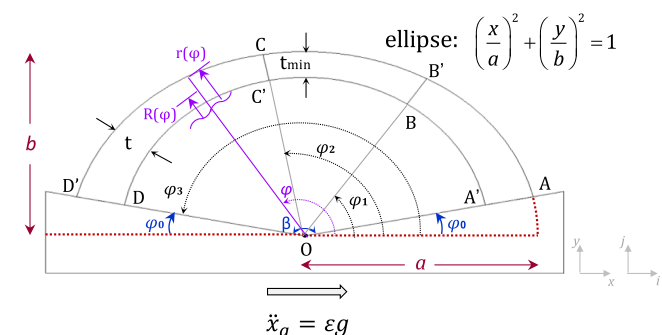$$

$$\qquad (20)$$

Fig. 4. Schematic of the part-elliptical arch.

$$t(\varphi) = R_e(\varphi) - R_i = \frac{b}{\sqrt{1 - \frac{a^2 - b^2}{a^2}cos^2\varphi}} - R_i \qquad (18)$$

in which, R_e and R_i are the external and internal radii respectively.

Similar to the circular case, when a critical horizontal acceleration $\ddot{x}_g = \varepsilon\,g$ is applied at its supporting base, the arch transforms into a four-hinge mechanism. The presumable hinge locations A, B, C, D defined by the angles φ_0, φ_1, φ_2, and φ_3 respectively are illustrated in the schematic of Fig. 4. Hinge A forms at the right extrados of the springing at position $\varphi_0 = (\pi - \beta)/2$ while hinge D is bounded by an unknown location φ_3. In this work a two-springing collapse mechanism is studied which means that hinge D forms at the intrados left springing (position $\varphi_3 = \pi - \varphi_0$). On the other hand, hinges B and C lie on the intrados and the extrados of the arch respectively.

3.2. Stability analysis

3.2.1. Variational formulation

Equilibrium analysis is applied for the segments formed, as described above. Each segment is characterised by its weight W and the co-ordinates of the centre of gravity x_{cm}, y_{cm} (Fig. 5). Alike the circular arch case, the cartesian components of the internal thrust force T_c (T_{c_x}, T_{c_y}) acting at the hinge C are considered as the unknown parameters of the equations below.

For segment 2 (BC), its weight W_2 and the centre of gravity (x_2, y_2) yield:

$$W_2 = \rho g \frac{1}{2}\left[(\varphi_1 - \varphi_2)(r'-1)^2 + \frac{(r'+1)^2\left(\pi - tan^{-1}\left(\frac{tan\varphi_1}{\lambda}\right) + tan^{-1}\left(\frac{tan\varphi_2}{\lambda}\right) \right)}{\lambda} \right] \qquad (19)$$

in which, r' is the slenderness ratio $t/2R$, and λ is the width-to-the-height ratio of the ellipse b/a. Likewise, for segment 3 (CD) its weight W_3 and the centre of gravity (x_3, y_3) yield:

$$W_3 = \rho g \frac{1}{2}\left[(\varphi_2 - \varphi_3)(r'-1)^2 - \frac{(r'+1)^2\left(tan^{-1}\left(\frac{tan\varphi_2}{\lambda}\right) - tan^{-1}\left(\frac{tan\varphi_3}{\lambda}\right) \right)}{\lambda} \right] \qquad (21)$$
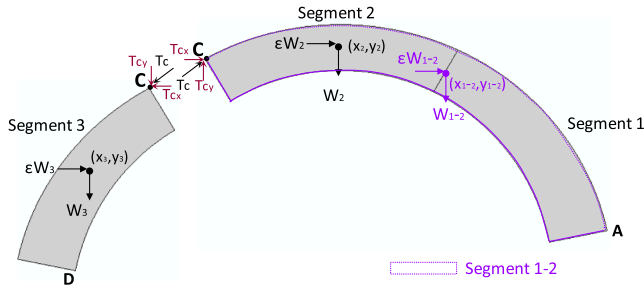
Fig. 5. Limit equilibrium analysis applied to the part-elliptical arch.

Likewise, moment equilibrium of (i) segment 2 (*BC*) around hinge *B* and (ii) segment 2 (*CD*) around hinge *D* yields Eqs. (26) and (27) respectively:

$$T_{c_x}\left(\frac{R(1+r')\sin\varphi_2}{\sqrt{1-\varepsilon^2\cos^2\varphi_2}}-R(1+r')\sin\varphi_1\right)+T_{c_y}\left(R(1+r')\cos\varphi_1-\frac{R(1+r')\cos\varphi_2}{\sqrt{1-\varepsilon^2\cos^2\varphi_2}}\right)$$
$$+\varepsilon W_2(y_2-R(1+r')\sin\varphi_1)+W_2(x_2-R(1+r')\cos\varphi_1)=0 \qquad (26)$$

$$T_{c_x}\left(\frac{R(1+r')\sin\varphi_2}{\sqrt{1-\varepsilon^2\cos^2\varphi_2}}-\frac{R(1+r')\sin\varphi_0}{\sqrt{1-\varepsilon^2\cos^2\varphi_0}}\right)+T_{c_y}\left(\frac{R(1+r')\cos\varphi_0}{\sqrt{1-\varepsilon^2\cos^2\varphi_0}}-\frac{R(1+r')\cos\varphi_2}{\sqrt{1-\varepsilon^2\cos^2\varphi_2}}\right)$$
$$+\varepsilon W_3\left(y_3-\frac{R(1+r')\sin\varphi_0}{\sqrt{1-\varepsilon^2\cos^2\varphi_0}}\right)+W_3\left(x_3-\frac{R(1+r')\cos\varphi_0}{\sqrt{1-\varepsilon^2\cos^2\varphi_0}}\right)=0 \qquad (27)$$

The subtraction of the potential energy of a purely elliptical (V_{el}) and

$$x_3=\frac{\left[-(r'-1)^3(\sin\varphi_2-\sin\varphi_3)+\dfrac{(1+r')^3\left(\dfrac{\tan\varphi_2}{\sqrt{\lambda^2+\tan\varphi_2{}^2}}-\dfrac{\tan\varphi_3}{\sqrt{\lambda^2+\tan\varphi_3{}^2}}\right)}{\lambda^2}\right]}{3W_3}$$

$$y_3=\frac{\left[-(r'-1)^3(\cos\varphi_2-\cos\varphi_3)+\dfrac{(1+r')^3\left(\dfrac{1}{\sqrt{\lambda^2+\tan\varphi_2{}^2}}-\dfrac{1}{\sqrt{\lambda^2+\tan\varphi_3{}^2}}\right)}{\lambda^2}\right]}{3W_3} \qquad (22)$$

For the combined segment 1–2 (*ABC*) its weight $W_{1\text{-}2}$ and the centre of gravity ($x_{1\text{-}2}$, $y_{1\text{-}2}$) yield:

$$W_{1-2}=\rho g\frac{1}{2}\left[(\varphi_0-\varphi_2)(r'-1)^2+\frac{(r'+1)^2\left(\pi-\tan^{-1}\left(\frac{\tan\varphi_0}{\lambda}\right)+\tan^{-1}\left(\frac{\tan\varphi_2}{\lambda}\right)\right)}{\lambda}\right] \qquad (23)$$

$$x_{1-2}=\frac{\left[-(r'-1)^3(\sin\varphi_0-\sin\varphi_2)+\dfrac{(1+r')^3\left(-\dfrac{\tan\varphi_0}{\sqrt{\lambda^2+\tan\varphi_0{}^2}}-\dfrac{\tan\varphi_2}{\sqrt{\lambda^2+\tan\varphi_2{}^2}}\right)}{\lambda^2}\right]}{3W_{1-2}}$$

$$y_{1-2}=\frac{\left[-(r'-1)^3(\cos\varphi_0-\cos\varphi_2)+\dfrac{(1+r')^3\left(-\dfrac{1}{\sqrt{\lambda^2+\tan\varphi_0{}^2}}-\dfrac{1}{\sqrt{\lambda^2+\tan\varphi_2{}^2}}\right)}{\lambda}\right]}{3W_{1-2}} \qquad (24)$$

Moment equilibrium of the combined segment 1–2 (*ABC*) around hinge *A* yields:

$$T_{c_x}\left(\frac{R(1+r')\sin\varphi_2}{\sqrt{1-\varepsilon^2\cos^2\varphi_2}}-\frac{R(1+r')\sin\varphi_0}{\sqrt{1-\varepsilon^2\cos^2\varphi_0}}\right)+T_{c_y}\left(\frac{R(1+r')\cos\varphi_0}{\sqrt{1-\varepsilon^2\cos^2\varphi_0}}-\frac{R(1+r')\cos\varphi_2}{\sqrt{1-\varepsilon^2\cos^2\varphi_2}}\right)$$
$$+\varepsilon W_{1-2}\left(y_{cm}^{1-2}-\frac{R(1+r')\sin\varphi_0}{\sqrt{1-\varepsilon^2\cos^2\varphi_0}}\right)+W_{1-2}\left(x_{cm}^{1-2}-\frac{R(1+r')\cos\varphi_0}{\sqrt{1-\varepsilon^2\cos^2\varphi_0}}\right)=0 \qquad (25)$$

a purely circular (V_c) arch gives the potential energy of this particular arch geometry (see Appendix A):

$$V=g\rho\frac{2R^3}{3}\left(\frac{(1+r')^3}{\sqrt{1-\varepsilon^2\cos^2\varphi_0}}-(1-r')^3\right)\cos\varphi_0 \qquad (28)$$

Next, the principle of stationary potential energy is revisited. Equilibrium is achieved when the potential energy is stationary meaning that the partial derivatives with respect to the critical angles φ_1, φ_2, φ_3, are equal to zero (Eq. (29)). By differentiating Eq. (28) with respect to the angles φ_i yields:

$$\frac{\partial V}{\partial\varphi_i}=\frac{dV}{dr'}\frac{\partial r'}{\partial\varphi_i}=0$$
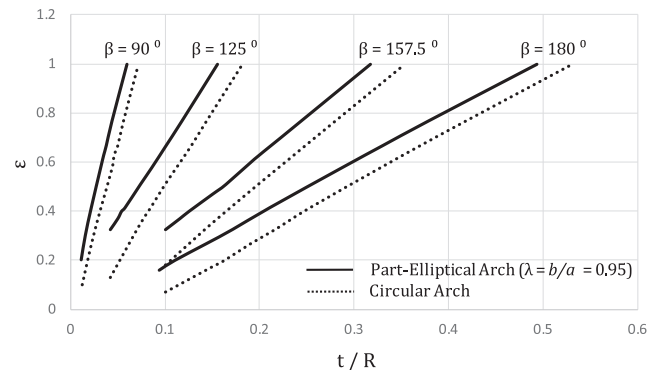$$\frac{\partial r'}{\partial\varphi_i}=0, i=1,2,3 \qquad (29)$$

Fig. 6. Seismic coefficient ε of circular arch and part-elliptical arch ($\lambda=b/a=0.95$) for given angles of embrace β corresponding to different slenderness t/R.
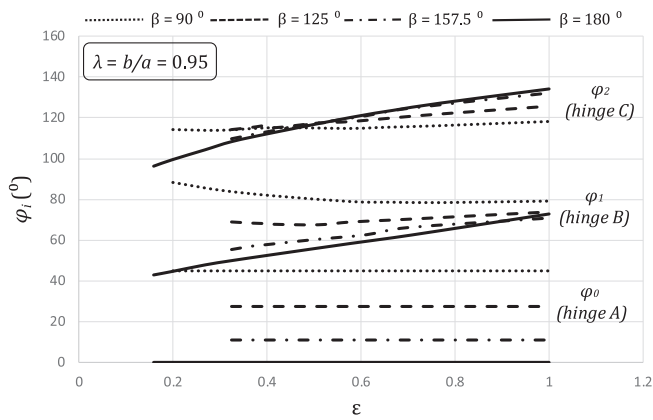
Fig. 7. Location of the imminent hinges φ_i where i = 0, 1, 2 (points A, B and C respectively) of a part-elliptical arch ($\lambda = b/a = 0.95$) with a given angle of embrace β.

Evidently, Eqs. (25)–(27) are implicit functions of the independent variables (the slenderness ratio r' and the acceleration ε as well as the dependent variable φ_i). Iterative procedures available in the code *Mathematica* are implemented to separate the dependent variable φ_i from r' and ε and therefore to derive the locus of the solution. The solution leads to the unknown locations of the ruptures $\varphi_{1,2}$ as well as the minimum thickness t/R for given angles of embrace.

Fig. 6 depicts comparatively a circular and a part-elliptical ($\lambda = b/a = 0.95$) arch for different levels of slenderness t/R and uplift acceleration εg, in terms of the critical acceleration needed to initiate motion. In particular, Fig. 6 implies that for a given slenderness, higher acceleration values are required to initiate uplift of a part-elliptical arch compared to those required for a circular one. In the first case, the slenderness t/R due to thickness variation is considered with regard to the smallest values of t (thickness) and R (radius). Each pair of curves with the same angle of embrace, has a lower bound determined by a minimum t/R and a common upper bound at $\varepsilon = 1$ (arbitrarily chosen). Fig. 7 illustrates the locations of hinges B and C forming when the arch is subjected to various values of uplift acceleration $\varepsilon\,g$, for given angles of embrace β. It is noted that the angle φ_0 depends only upon β ($\varphi_0 = [\pi - \beta]/2$). Interestingly, it is also observed that as confinement of the arch is gradually enforced (larger values of φ_0) the kinematic mechanism tends to be independent to the seismic coefficient, ε. On the other hand, for the unconfined arch ($\varphi_0 = 0$) a rather linear trend is established between the angles φ_1, φ_2 and the coefficient ε. The endpoints of the curves (minimum and maximum values of the seismic coefficient ε) are in one-to-one matching with the endpoints of the curves of Fig. 6. Fig. 8 yields that the ratio λ (=b/a) is linear to slenderness t/R for various levels of the seismic coefficient ε. It is confirmed that the arch thickness is favourable to the

stability of the structural system, in a way that higher acceleration levels are required to induce rocking as the thickness is gradually increasing. Moreover, when comparing two arches of the same slenderness t/R but of different angles of embrace β it is concluded that the one of larger β becomes a four-hinge mechanism for a larger horizontal acceleration εg.

A numerical example can further elucidate the interplay of the geometrical parameters and the acceleration required for incipient uplift. The numerical values are chosen from the graphs of Figs. 6 and 7. Let us consider the case where $\beta = 157.5°$ and $t/R = 0.194$. A circular arch uplifts for a horizontal ground acceleration, $\ddot{x}_g = 0.51$ g, whereas a part-elliptical one when $\ddot{x}_g = 0.61$ g. In the first case, hinges form at $\varphi_1 = 56.622°$, $\varphi_2 = 116.611°$ and $\varphi_3 = 168.75°$, whilst in the second case at $\varphi_1 = 62.6°$, $\varphi_2 = 121.076°$ and $\varphi_3 = 168.75°$. Other geometrical parameters are: (a) the mid-radius R ($R = 10$ m), the thickness t ($t/R = 0.194 => t = 1.94$ m), the external radius b ($b = R + t/2 = 10.971$ m) which are identical in both cases and (b) the ratio λ ($\lambda = b/a = 0.95$) and a ($a = b/\lambda = 10.971/0.95 = 11.5484$) which are additional for the part-elliptical arch (Fig. 4).

3.2.2. Lagrangian formulation

The kinematic mechanism in combination with the Lagrangian non-linear formulation can contribute to extract the governing equation of motion. To this extent, the Lagrangian equation can be expressed in the following compact form.

$$\frac{d}{dt}\left(\frac{\partial T}{\partial \dot{\theta}}\right) - \frac{\partial T}{\partial \theta} + \frac{\partial V}{\partial \theta} = Q \tag{30}$$

in which, T is the kinetic energy of the system, V the potential energy and Q the generalized forces. For this single-degree-of-freedom system
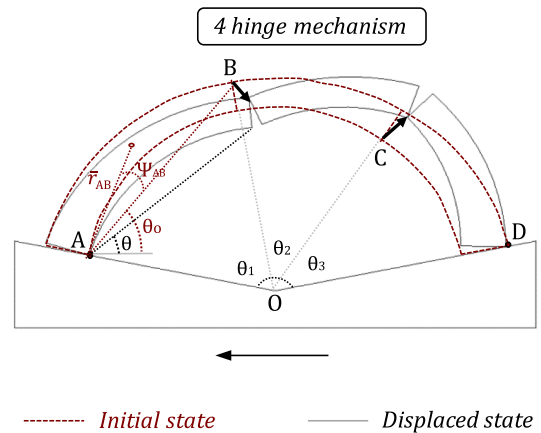

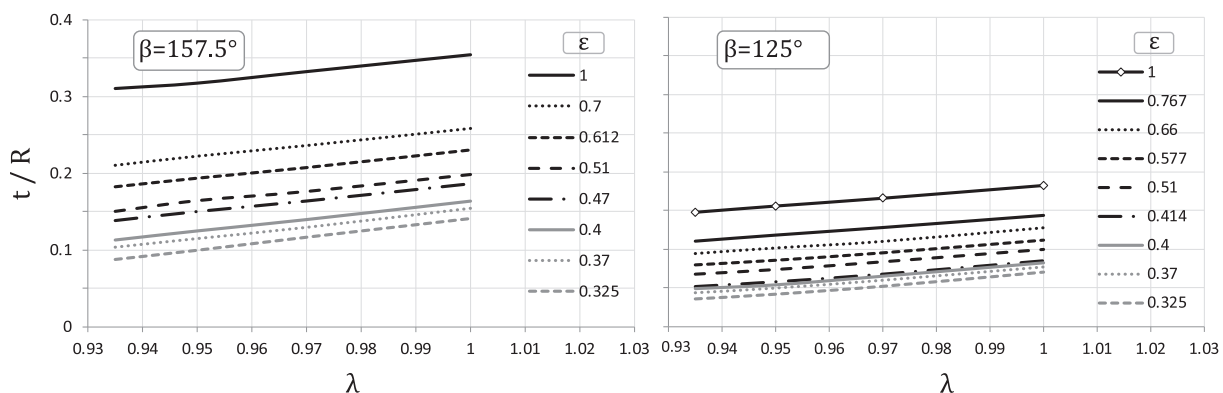**Fig. 9.** Kinematic mechanism of the part-elliptical arch.

Fig. 8. Minimum required slenderness as a function of $\lambda = b/a$ for different levels of the uplift horizontal acceleration $\ddot{x}_g = \varepsilon g$.

the angle $\theta = \theta_{AB} = \theta_0$ is chosen arbitrarily and without violating the constraint, as the Lagrangian independent variable (coordinate).

The kinematics of the system employed to formulate the Lagrangian equation of motion is portrayed in Fig. 9. The horizontal supporting base is represented with a rigid plane free to undergo horizontal vibration. The rocking arch consists of 3 rigid segments (AB, BC, CD) that correspond to different portions of the angle of embrace β ($=\theta_1 + \theta_2 + \theta_3$). The initial and the displaced state are determined with the angles θ_0 and θ respectively measured anticlockwise from the horizontal. The rotation of such a system, is denoted as ϕ, is $\theta_0 - \theta$ with respect to the original geometry. The horizontal acceleration applied to the base from right to left ($\ddot{x}_g < 0$) causes a positive rotation (ϕ) of the arch which initially will rock to the right.

Consequently, the equation of motion takes the compact form:

$$M(\theta)\ddot{\theta} + L(\theta)\dot{\theta}^2 + F(\theta)g = P(\theta)\ddot{x}_g \quad (31)$$

in which the coefficients $M(\theta), L(\theta), F(\theta), P(\theta)$ are nonlinear equations of θ given below after replacing $f_{xy} = m_{xy}\bar{r}_{xy}^2 + I_{xy}$. Where $m_{xy}, \bar{r}_{xy}, I_{xy}$ and ψ_{xy} are the mass, the distance to the centre of mass measured from the downstream joint corresponding to each link, the centroidal polar moment of inertia and the angular offset respectively ($xy = AB, BC, CD$) (Fig. 9).

$$M(\theta) = f_{AB} + f_{BC}\theta_{BC}'^2 + f_{CD}\theta_{CD}'^2 + m_{BC}\left[AB^2 + 2AB\bar{r}_{BC}\theta_{BC}'\cos(\theta - \theta_{BC}\right.$$
$$\left. - \psi_{BC})\right] \quad (32)$$

$$L(\theta) = f_{BC}\theta_{BC}'\theta_{BC}'' + f_{CD}\theta_{CD}'\theta_{CD}'' + m_{BC}AB\bar{r}_{BC}[\theta_{BC}''\cos(\theta - \theta_{BC} - \psi_{BC}) - \theta_{BC}'(1$$
$$- \theta_{BC}')\sin(\theta - \theta_{BC} - \psi_{BC})] \quad (33)$$

$$F(\theta) = m_{AB}\bar{r}_{AB}\cos(\theta + \psi_{AB}) + m_{BC}[AB\cos\theta + \bar{r}_{BC}\theta_{BC}'\cos(\theta_{BC}$$
$$+ \psi_{BC})] + m_{CD}\bar{r}_{CD}\theta_{CD}'\cos(\theta_{CD} + \psi_{CD}) \quad (34)$$

$$P(\theta) = m_{AB}\bar{r}_{AB}\sin(\theta + \psi_{AB}) + m_{BC}[AB\sin\theta + \bar{r}_{BC}\theta_{BC}'\sin(\theta_{BC}$$
$$+ \psi_{BC})] + m_{CD}\bar{r}_{CD}\theta_{CD}'\sin(\theta_{CD} + \psi_{CD}) \quad (35)$$

These functions have been presented in literature in similar forms [6,7,19]. In addition, their physical interpretation has also been elucidated [6]. Eq. (31) is valid only when $\theta < \theta_o$, meaning that the computation of the rocking angle θ is limited to the prior-to-impact state. Evidently, the equation of motion is dependent upon the geometrical characteristics of the structure. A similar procedure has been followed for a circular arch [6,7,19]. Nevertheless, the part-elliptical arch requires a larger computational effort due to geometric complexities. The horizontal ground acceleration needed to initiate
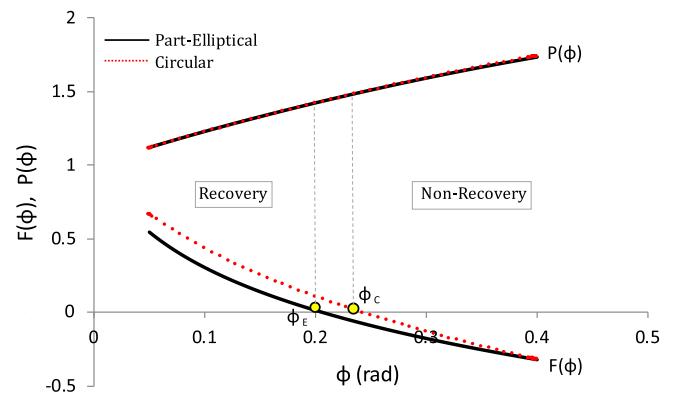

Fig. 10. Recovery and non-recovery domain introduced by the normalised potential energy for both circular and part-elliptical arch (dotted and continuous lines respectively).

Fig. 11. Representative coefficients F and P defined by the non-recovery point for circular and part-elliptical arch (dotted and continuous lines respectively).

uplifting about the predefined hinges can also be extracted from Eq. (31) by applying the criterion for incipient rocking: $\ddot{\theta} = \dot{\theta} = 0$. The above condition states that the supporting base should experience acceleration larger than $\left|\ddot{x}_g\right| = F(\theta)/P(\theta) = 0.61$ g in order the developing inertia forces to set the arch on rocking. Compared to the circular arch case where $\left|\ddot{x}_g\right| = F(\theta)/P(\theta) = 0.51$ g, the part-elliptical arch performs enhanced-resistance to entering the rocking mode. The above values of uplift acceleration can also be extracted from the diagram of Fig. 6.

A comparison between the part-elliptical and the circular arches is performed in Fig. 10 in terms of the potential energy normalised to its value as a function of the rotation ϕ. A turning point of the system is at the moment the potential energy reaches its peak value which corresponds to maximum rotation ϕ_c and ϕ_e for the circular and part-elliptical arch respectively. For these critical values of rotation, velocity and kinetic energy are instantaneously zero and the system "decides" whether it eventually collapses or not. For the circular case the point of non-recovery is reached after a relatively small rotation. In fact, as already pointed out by Oppenheim [6] "*a typical arch has considerable resistance to the onset of mechanism motion but relatively little capacity to absorb forced excursions into such motion*". This finding is even more amplified in the part-elliptical arch in which the critical rotation ϕ drops from 0.25 rad down to 0.20 rad at a maximum energy ratio $V(\phi)/V(\phi_0)$ even higher.

For a rocking masonry arch, gravity is the restoring mechanism that brings the structure back to static equilibrium. In Fig. 11, both the restoring and the driving mechanism for each profile are portrayed. The alternation of sign in the case of the coefficient $F(\theta)$ denotes that the mechanism the gravitational force imposes to the system turns from restoring to driving. For the part-elliptical arch (continuous line) gravity leads the system to overturning faster compared to the circular arch (dotted line). Therefore, the point of non-recovery ϕ_{cr} is reached earlier in the first case. This is a reasonable finding as the part-elliptical arch is heavier, due to its geometry. On the other hand, during the entire motion, the ground acceleration contributes to the system as a destabilising factor. In concluding, a circular arch requires smaller acceleration amplitudes to uplift while the part-elliptical exhibits substantial resistance to earthquake pulses. On the other hand, the part-elliptical arch reaches the threshold of collapse in smaller rotations than the circular arch for a specific thickness/radius ratio.

3.3. Time-history analysis

3.3.1. Lagrangian formulation

The governing equation of motion as derived from Lagrangian formulation (Eq. (31)) in combination with the nonlinear coefficients (Eqs. (32)–(35)) is implemented to compute the time-history of rocking
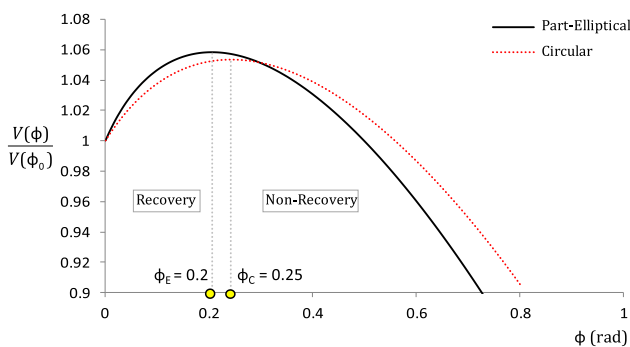
rotation. A numerical solution of the differential equation of motion in terms of rotation ϕ (or the angle θ) is accomplished with *Mathematica* code, after properly adjusting the coefficient $P(\phi)$ (or $P(\theta)$) to implement ground shaking. The linearised equation of motion is solved iteratively through a numerical solver (ND solve) in the Wolfram Mathematica 8 environment. To determine the solutions of the equation, initial conditions are denoted in the form $\phi(0) = 0$ and $\phi'(0) = 0$. Mathematica can switch methods many times if the situation asks for it. The explicit integration settings for the applied methods are the "Runge-Kutta" (Implicit or Explicit), the "Adams" methods or implicit backward differentiation formulas (BDF or IDA).

3.3.2. Finite element modelling

Nonlinear analysis of a free-standing arch on accelerating base is implemented numerically in the time-domain with the finite element method. To this extent, the software suite *Abaqus* [27] is utilised for the mesh generation as well as for the analysis execution. Both the arched structure and the supporting base are represented with quadrilateral, continuum plain strain elements. A reasonably refined mesh of the model is generated, composed of elements varying from 0.33 m to 0.47 m in width for the arch and from 0.17 m to 0.39 m for the base. The linearly elastic behaviour of the masonry arch is determined by elastic modulus, $E = 10$ GPa, Poisson ratio, $\nu = 0.20$, and density, $\rho = 2.2$ t/m^3. In the same way, for the supporting base the material properties are $E = 30$ GPa, $\nu = 0.20$, and $\rho = 2.5$ t/m^3. For such high levels of the elastic moduli, flexural deformations are rather negligible, and therefore each structural element can practically be considered as rigid. The arch is partitioned in three monolithic voussoirs which together with the base form four interfaces (hinges). A surface-based kinematic contact algorithm has been adopted allowing for rigorous treatment of finite separation (uplifting) and sliding at each interface. The latter is governed by a Coulomb-type frictional law at the interface. Experimental studies have pointed out that for masonry stones the coefficient of friction can roughly be estimated at 0.7 [28]. Geometric nonlinearity attributed to $P-\delta$ effects is taken into account through appropriate large displacement formulation. A direct integration of the equations of motion is performed at each time increment through an explicit algorithm incorporated in the finite element code. This dynamic analysis procedure is based upon the implementation of the explicit central-difference integration rule of the kinematic variables (Eq. (36)):

$$\dot{u}^N_{\left(i+\frac{1}{2}\right)} = \dot{u}^N_{\left(i-\frac{1}{2}\right)} + \frac{\Delta t_{(i+1)} + \Delta t_{(i)}}{2}\ddot{u}^N_{(i)} ,$$

$$u^N_{(i+1)} = u^N_{(i)} + \Delta t_{(i+1)}\dot{u}^N_{\left(i+\frac{1}{2}\right)} , \qquad (36)$$

Fig. 13. One-sine pulse (cycloidal Type A pulse).

where u^N is a degree of freedom (a displacement or rotation component) and the subscript i refers to the increment number. In addition, the use of diagonal ("lumped") element mass matrices allows for the accelerations at the beginning of the increment to be computed according to Eq. (37).

$$\ddot{u}^N_{(i)} = \left(M^{NJ}\right)^{-1}\left(P^J_{(i)} - I^J_{(i)}\right) \qquad (37)$$

where M^{NJ} is the mass matrix, $P^J_{(i)}$ is the applied load vector, and $I^J_{(i)}$ is the internal force vector. The afore-discussed explicit procedure is computationally efficient in a sense that it requires no iterations and no tangent stiffness matrix. The computational cost is further minimised by choosing reduced integration elements (CPE4R) available in Abaqus/Explicit code. The finite element configuration of the model is illustrated in Fig. 12.

The lateral boundaries of the model are free to move horizontally unlike the vertical movement of the base which is restricted. Concerning the horizontal loading, different types of pulses are in all cases uniformly imposed to the bottom surface of the base for representing seismic excitation. On the other hand, vertical loading is restricted to the self-weight of the structure excluding the effect of other gravitational loads caused by the backfill or live loads.

3.3.3. Comparative study

Effect of the non-uniform profile. The response of the part-elliptical arch is first computed with the finite element method for different levels of geometrical ratio λ. In this way the results can be comparatively presented with those of the circular arch ($\lambda = 1$). A series of one-cycle trigonometric pulses is applied as excitation at the base. This sort of pulses approximates the kinematic characteristics of recorded near-source excitations and may lead to considerable permanent displacements. They are discretised to Type A (forward pulse or one sine pulse), Type B (forward-and-back pulse or cosine pulse) and Type C$_n$
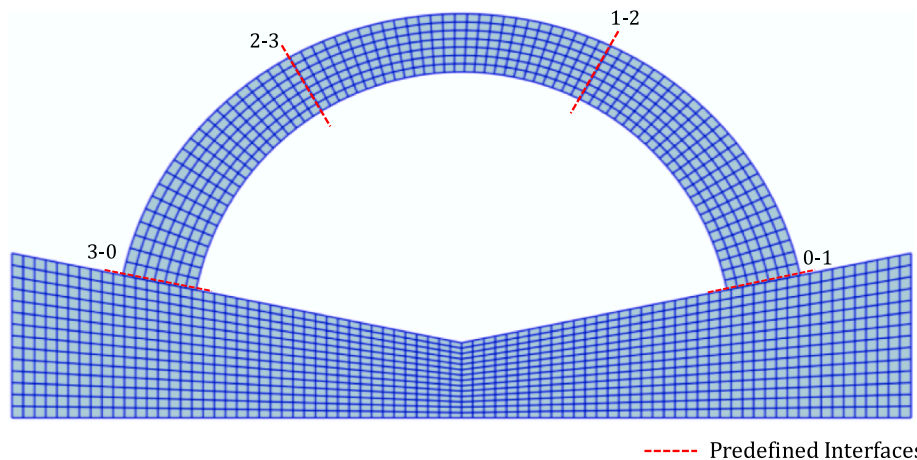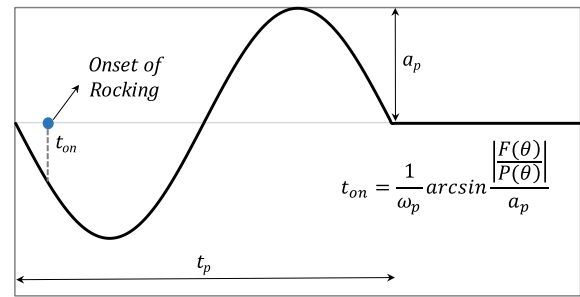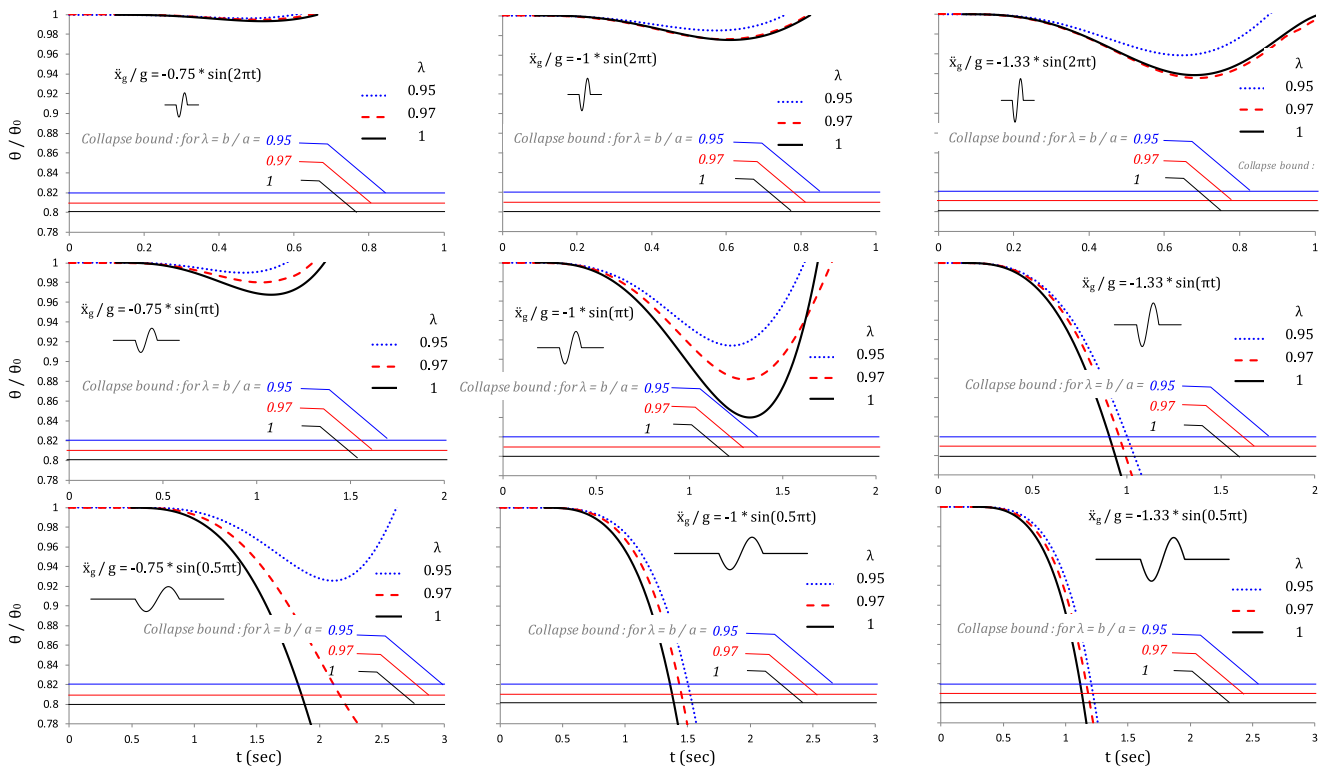

------ Predefined Interfaces

Fig. 12. 2-dimensional finite element model of the non-uniform arch and the supporting base. The four predefined interfaces are also depicted.

Fig. 14. The influence of the geometrical ratio λ on the time history of the normalised angle θ when the arch is subjected to various one-sine pulses. Three different cases are investigated: (a) for λ = 0.95 (part-elliptical arch), (b) λ = 0.97 (part-elliptical arch) and c) λ = 1 (circular arch). Collapse bounds for each case are depicted.
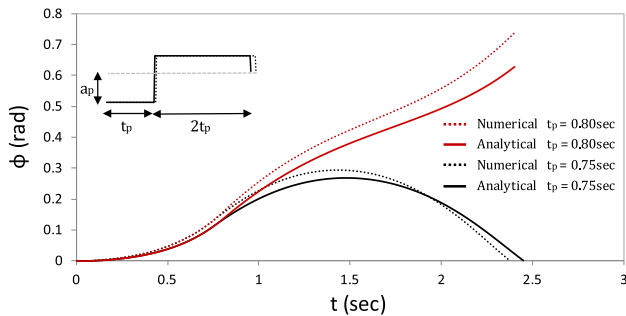

Fig. 15. Rotation time histories of the part-elliptical arch subjected to different rectangular pulses. Black lines: $t_p = 0.75$ s. Red lines: $t_p = 0.80$ s. Solid lines: analytical solution. Dashed lines: numerical solution. (For interpretation of the references to colour in this figure legend, the reader is referred to the web version of this article.)

(exhibits n cycles). The present study is limited to the first type due to its more detrimental effects. This so-called one-sine pulse is presented in Fig. 13. It is characterised by the amplitude a_p, the period T_p, and the time for the onset of rocking t_{on} expressed in terms of amplitude a_p,

frequency $\omega_p = \frac{2\pi}{T_p}$, and the ratio $F(\theta)/P(\theta)$. Fig. 14 portrays time-histories of the normalised angle, θ, for three different values of λ: 0.95, 0.97, 1. Hence, three arches of different upper curve (extrados) are selected, in which the minor axis ($b = 10.97$ m) is kept constant whereas the value of the major axis (a) ranges from $a = b = 10.97$ m (circular case) to $a = 11.31$ m and $a = 11.5484$ m (elliptical cases). In light of the above, a salient comparison among the three arches can be performed. During arch rocking, two different states can be distinguished: (a) rocking with impact during the excitation or (b) overturning at the first half of the cycle. For high frequency pulses ($\omega_p = 2\pi$) the increase in the acceleration amplitude, from 0.75 g to 1 g and eventually to 1.33 g, doesn't essentially affect the arch behaviour for any of the arches. For lower values of frequency ω_p (π, 0.5π) though, the acceleration amplitude plays a crucial role to the arch response. For instance, a pulse of $\omega_p = \pi$ may lead to collapse for $a_p = -1.33$ g whereas for lower amplitudes the arch survives failure. Another interesting response is the one caused by a pulse of $\omega_p = 0.5\pi$ and $a_p = -0.75$ g where the arch of $\lambda = 0.95$ manages to survive failure unlike the other two arches. The following one-cycle pulses induce larger rotations for circular arches which in some cases may lead to collapse. In view of the above findings, it may be stated that part-elliptical arches due to their slightly different geometry are more stable structures than the circular arches. Particularly the more
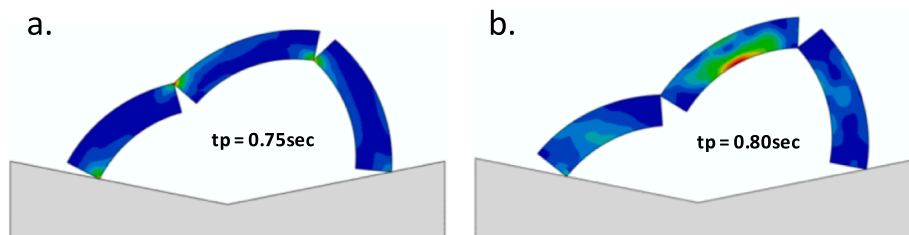

Fig. 16. Illustration of snapshots of the part-elliptical arch subjected to rectangular pulses. (a) Recover, $tp = 0.75$ s (left), (b) overturning, $tp = 0.80$ s (right).
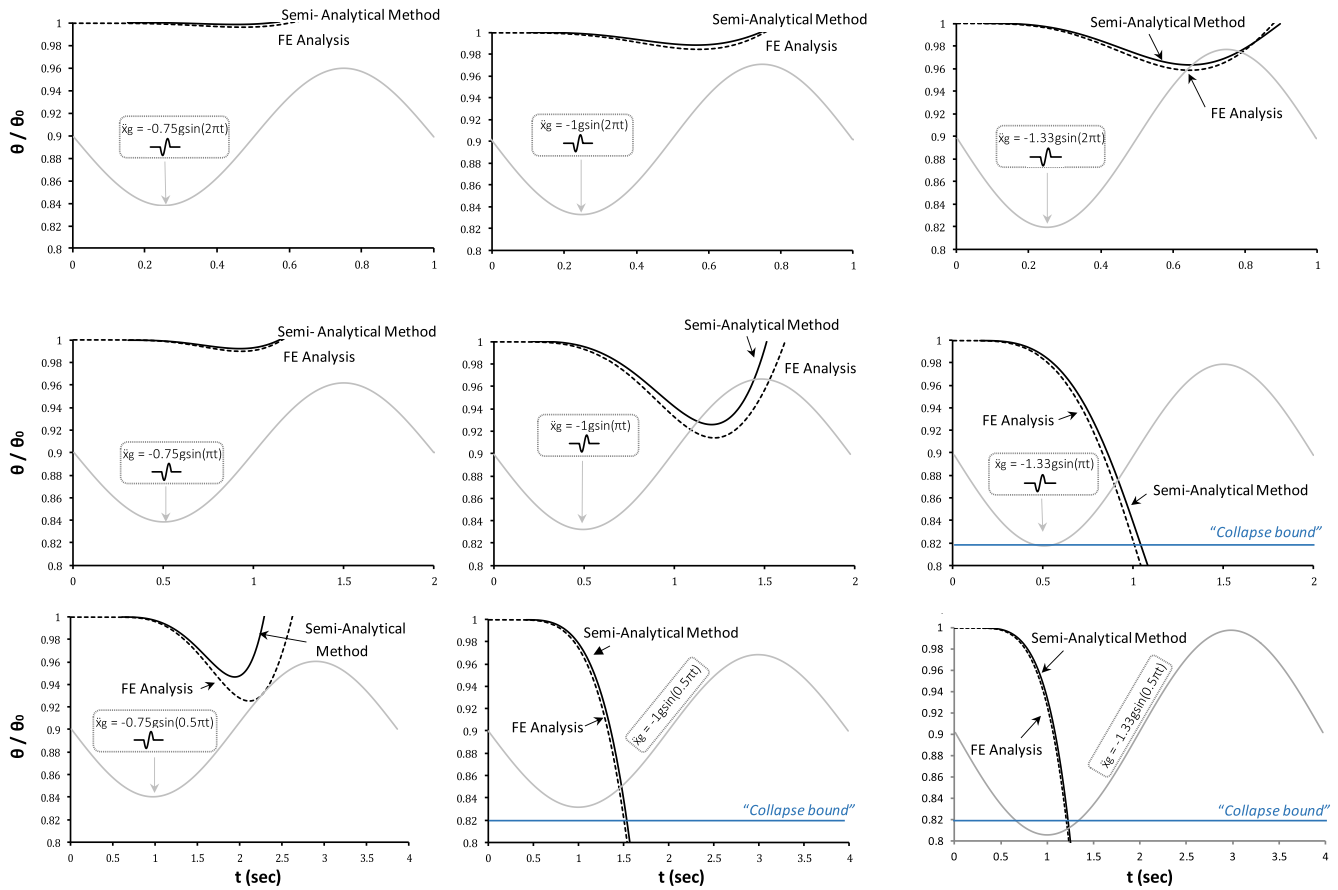
Fig. 17. Time histories of the normalised angle θ of a part-elliptical arch ($\lambda = 0.95$) excited by one-sine pulses at the base. Comparison between FE (dotted line) and semi-analytical solution (continuous line).

"elliptical" the upper curve is the less prone is the arch to failure. Their stability decreases as the geometrical ratio λ increases till the value of $\lambda = 1$ where the arch becomes circular.

Comparison between analytical and numerical solution. The results of the time-history analysis obtained with the semi-analytical method are comparatively presented next with those of the finite element method for a part-elliptical arch with geometrical ratio $\lambda = 0.95$. Such a comparison is essential due to the assumptions and simplifications involved in these two methods. Hence, the analytical approach adopts the rigid, no-tension model of a monolithic arch in which sliding along the joints is prevented. On the other hand, the finite element approach considers for the masonry a very stiff structure ($E = 30$ GPa), yet not ideally rigid. In addition, the imminent hinges are predefined as a prevailing kinematic mechanism under dynamic lateral load is regarded, whereas sliding is not prevented. A two-step rectangular pulse is introduced to the analysis as an excitation to the supporting base. It contains a large negative pulse ($a_p = -1$ g) of duration t_p followed by a smaller positive pulse of half magnitude ($a_p = 0.5$ g) and of double duration $2t_p$. Such pulses were introduced to the analyses and used in recent studies [5,6,9]. Their particularity is the lack of residual velocity. In Fig. 15, the arch response to pulses with duration $t_p = 0.75$ s and $t_p = 0.80$ s is illustrated using both the analytical and the numerical method. For a pulse of $t_p = 0.75$ s as a base motion (black lines), the arch safely exhibits rocking and returns to equilibrium state (rotation $\phi = 0$ rad) regardless of the method, analytical or numerical (solid or dotted line respectively). On the contrary, for a pulse of $t_p = 0.80$ s (red lines) both solutions predict that the arch is rocking and eventually overturns as rotation ϕ increases exponentially. More importantly, a good agreement is also observed between analytical and numerical solution for both pulses. A sequence of snapshots resulted from the deformed FE

mesh model is portrayed in Fig. 16. These snapshots portray the arch in the last increment of the pulse (state of recover and overturning).

The comparative study of the two methods implemented to compute rocking response is extended next as illustrated in Fig. 17. To this end, the part-elliptical arch of the numerical example of Section 3.2.1 is once more adopted ($\beta = 157.5°$ and $t/R = 0.194$). Ground motion applied to the supporting base is simulated with a one-sine pulse of acceleration amplitude values 0.75 g, 1.0 g, and 1.33 g. It is worthy of note that all three values exceed the threshold acceleration at incipient uplift (0.61 g), hence rocking motion is expected. In addition, three values of the excitation period are adopted: 1.0 s, 2.0 s, 4.0 s. The above values of a_p and T_p form a set of 9 analyses, all representative of very strong motion under quasi-static conditions. A remarkable agreement between the two methods is observed, which highlights the reliability of both approaches in the context of a dynamic time-history analysis. A slight deviation is observed in the case of $\omega_p = 0.5\pi$ and $a_p = 0.75$ g where the semi-analytical method gives more conservative results.

4. Conclusions

An arch ring of non-uniform thickness subjected to rocking is employed in this study. This so-called part-elliptical arch is described with an elliptical (upper) and a circular (lower) curve, and is frequently encountered in long-span masonry bridges. The paper investigates the response of such a structure in comparison with the uniform circular arch.

Based on the existing method of a variational formulation in literature [3], in the beginning the paper calculates the hinge locations of a continuous monolithic circular arch when subjected to a given level of acceleration $\ddot{x}_g$. What is new in this study is that the locations of the

imminent hinges are calculated analytically through closed-form solutions. The results are in excellent agreement with those derived from the semi-analytical approach of previous study [3].

Regarding the part-elliptical arch, (i) stability analysis and (ii) dynamic response analysis are engaged. Stability analysis involves both variational and Lagrangian formulation. In the context of a demand assessment, namely for a given slenderness, it is found that systematically higher acceleration levels are required to set a part-elliptical arch on rocking compared to those required for a circular one. This implies that an arch with increasing thickness from the key to the springers (as described with λ) performs enhanced resistance to hinge formation and rocking when subjected to ground horizontal excitation. Therefore, it has reasonably been adopted in the past as an improved profile in terms of seismic performance, for long-span masonry bridges. Moreover, when comparing two arches of the same slenderness t/R but of different angles of embrace β it is concluded that the one of larger β becomes a four-hinge mechanism for a higher horizontal acceleration ε g. Dynamic response analysis is performed in the time domain through analytical and numerical methods. In the former, time-histories of the rocking response are computed from the analytical solution of the Lagrangian equation of motion. Idealised pulses are used as base excitation to represent conditions of near-source ground shaking. Once rocking occurs it turns out that the non-uniform profile impacts the response but not in a straightforward fashion. Evidently, the response is very sensitive to the excitation period unveiling the profoundly non-linear nature of the problem. Apart from the analytical treatment, two-dimensional numerical analysis with finite elements is performed. The results are presented comparatively with those of the analytical method for long-duration pulses. Both methods provide time-histories of the dynamic response which in general lines are in remarkable agreement. This is very important taking into account the essentially different assumptions adopted in two approaches: The analytical method considers a rigid, monolithic arch of zero tensile strength in which sliding at the joints is prevented. On the contrary, the numerical model implies a stiff but not ideally rigid structure with a predefined hinge mechanism, where interfaces are reasonably rough allowing theoretically sliding.

It has to be mentioned that in the analyses presented herein only dead loads due to the arch ring weight have been considered neglecting additional gravity loads mainly due to backfill or overburden material. This simplifying approach is conservative and allows for the comparison with a plethora of previous studies already presented in literature on the pure arch behaviour [3–20,22,23–25]. A more realistic simulation of the arch as a part of a structure (e.g bridge, entrance, vault) is a topic for future research. A complete masonry arch configuration could be implemented, including apart from the arch ring, the spandrel structure and the fill material above. The development of the semi-analytical method could expand taking into consideration more complicated loading and boundary conditions. The presence of spandrels, backfill soil, and piers is expected to strongly affect the arch stress distribution and its load-bearing capacity [21,23,29,30,31]. Finally, regarding the finite element model, the analysis can be extended in a future study to address a monolithic, no-tension arch.

CRediT authorship contribution statement

Aikaterini Leontari: Conceptualization, Methodology, Software, Formal analysis, Writing - original draft, Writing - review & editing. **Marios Apostolou:** Conceptualization, Writing - original draft, Writing - review & editing, Visualization, Supervision.

Declaration of Competing Interest

The authors declare that they have no known competing financial interests or personal relationships that could have appeared to influence the work reported in this paper.

Appendix A

Algebraic manipulations to derive Eq. (28).

Potential Energy of the solid surface determined by the elliptical upper curve of the arch (ACD′), and the segments (OA), (OD′) as illustrated in Fig. 4:

$$V_{el} = \int dV = g\rho \iint (r\sin\varphi)rdrd\varphi = \frac{(ab)^3}{3}g\rho\int_{\varphi_1}^{\varphi_2} \frac{\sin\varphi d\varphi}{\left(\sqrt{b^2\cos^2\varphi + a^2\sin^2\varphi}\right)^3} = g\rho\frac{ab^3}{3}\left(\frac{1}{\sqrt{b^2 + a^2 tan^2\beta_0}} - \frac{1}{\sqrt{b^2 + a^2 tan^2(\pi - \beta_0)}}\right) \quad \text{(A.1)}$$

Potential Energy of the solid surface determined by the circular lower curve of the arch (A′C′D), and the segments (OA′), (OD) as illustrated in Fig. 4:

$$V_{circ} = g\rho\int \sin\varphi d\varphi \int_0^c r^2 dr = g\rho\frac{\left(R - \frac{t}{2}\right)^3}{3}(\cos\varphi_1 - \cos\varphi_2) = g\rho\frac{c^3}{3}\left(cos^2\beta_0 - cos^2(\pi - \beta_0)\right) \quad \text{(A.2)}$$

The Potential Energy of the part-elliptical arch is derived by subtracting A.2 from A.1, namely:

$$V_{el} = g\rho\frac{ab^3}{3}\left(\frac{1}{\sqrt{b^2 + a^2 tan^2\beta_0}} - \frac{1}{\sqrt{b^2 + a^2 tan^2(\pi - \beta_0)}}\right) - g\rho\frac{c^3}{3}\left(cos^2\beta_0 - cos^2(\pi - \beta_0)\right) = g\rho\frac{2R^3}{3}\left(\frac{(1 + r')^3}{\sqrt{1 - \varepsilon^2\cos^2\varphi_0}} - (1 - r')^3\right)\cos\varphi_0 \quad \text{(A.3)}$$

Appendix B. Supplementary material

Supplementary data to this article can be found online at https://doi.org/10.1016/j.engstruct.2020.111519.

References

[1] Couplet P. De la poussée des voûtes. Histoire de l' Académie Royale des Sciences. Académie Royale des Sciences. Paris; 1729.

[2] Milankovitch M. Beitrag zur theorie der druckkurven. Dissertation zur erlangung der Doktorwürde, K.K. Technische Hochschule. Vienna; 1904.

[3] Alexakis H, Makris N. Limit equilibrium analysis and the minimum thickness of circular masonry arches to withstand lateral inertial loading. Arch Appl Mech 2014;84:757–72.

[4] Alexakis H, Makris N. Minimum thickness of elliptical masonry arches. Acta Mech 2013;224:2977–91.

[5] Heyman J. The masonry arch. Chichester: Ellis Horwood; 1982.

[6] Oppenheim I. The masonry arch as a four-link mechanism under base motion. Earth Engng Struct Dyn 1992;21:1005–17.

[7] Clemente P. Introduction to dynamics of stone arches. Earthquake Engng Struct Dyn 1998;27:513–22.

[8] Ochsendorf J. Collapse of masonry structures. Department of Engineering. Cambridge: University of Cambridge; 2002.

[9] Dimitri R, Tornabene F. A parametric investigation of the seismic capacity from masonry arches and portals of different shapes. Engng Failure Anal 2015;52:1–34.

[10] Cavalagli N, Gusella V, Severini L. The safety of masonry arches with uncertain geometry. Comput Struct 2017;188:17–31.

[11] Di Carlo F, Coccia S, Rinaldi Z. Collapse load of a masonry arch after actual displacements of the supports. Arch Appl Mech 2018;88:1545–58.

[12] Zampieri P, Simoncello N, Pellegrino C. Seismic capacity of masonry arches with irregular abutments and arch thickness. Const Build Mat 2019;201:786–806.

[13] Stockdale G, Milani G. Diagram based assessment strategy for first-order analysis of masonry arches. J Build Engng 2019;22:122–9.

[14] Stockdale G, Sarhosis V, Milani G. Seismic capacity and multi-mechanism analysis for dry-stack masonry arches subjected to hinge control. B Earth Engng 2020;18:673–724.

[15] De Lorenzis L, DeJong M, Ochsendorf J. Failure of masonry arches under impulse base motion. Earth Engng Struct Dyn 2007;36(14):2119–36.

[16] Dimitrakopoulos E, DeJong M. Seimic overturning of rocking structures with external viscous dampers. Comp Methods Earth Engng 2013;30:243–58.

[17] De Santis S, de Felice G. A fibre-based approach for the evaluation of the seismic capacity of masonry arches. Earth Engng Struct Dyn 2014;43:1661–81.

[18] Gaetani A, Lourenco P, Monti G, Moroni M. Shaking table tests and numerical analyses on a scaled dry-joint arch undergoing windowed sine pulses. B Earth Engng 2017;15:4939–61.

[19] Leontari A, Apostolou M. Linearised response of arched structures under pulse-type excitation. Arch Appl Mech 2018;88(7):1121–37.

[20] Kollár L, Ther T. Numerical model and dynamic analysis of multi degree of freedom masonry arches. Earth Engng Struct Dyn 2019;48(7):709–30.

[21] Sarhosis V, Forgács T, Caddemi S, Lemos J. A discrete approach for modelling backfill material in masonry arch bridges. Comp Struct 2019;224:106108.

[22] Cannizzaro F, Pantó B, Caddemi S, Caliò I. A Discrete Macro-Element Method (DMEM) for the nonlinear structural assessment of masonry arches. Engng Struct 2018;168:243–56.

[23] Pulatsu B, Erdogmus E, Lourenco P. Comparison of in-plane and out-of-plane failure modes of masonry arch bridges using discontinuum analysis. Engng Struct 2019;178:24–36.

[24] Stockdale G, Sarhosis V, Milani G. Seismic capacity and multi-mechanism analysis for dry-stack masonry arches subjected to hinge control. Bull Earthq Engng 2020;18:673–724.

[25] Tempesta G, Galassi S. Safety evaluation of masonry arches. A numerical procedure based on the thrust line closest to the geometrical axis. Int J Mech Sc 2019;155:206–21.

[26] D' Agostino S & Bellomo M. Ponti in muratura e in calcestruzzo armato. Manuale di ingeneria Civile (Vol. II). Buologne: Zanichelli/ESAC; 2001.

[27] Abaqus. Theory and analysis user`s manual, version 6.8-3. Providence, RI, USA: Dassault Systèmes Simulia Corp; 2008.

[28] Marino M, Neri F, De Maria A, Antonio B. Experimental data of friction coefficient for some types of masonry and its correlation with an index of quality masonry (Iqm). In: 2nd European conference on earth Engng & Seism, Istanbul; 2014.

[29] Reccia E, Milani G, Checci A, Tralli A. Full 3D homogenization approach to investigate the behavior of masonry arch bridges: the Venice trans-lagoon railway bridge. Constr Build Mat 2014;66:567–86.

[30] da Porto F, Tecchio G, Zampieri P, Modena C, Prota A. Simplified seismic assessment of railway masonry arch bridges by limit analysis. Struct Infrstruct Engng 2016;12(5):567–91.

[31] Sarhosis V, De Santis S, de Felice G. A review of experimental investigations and assessment methods for masonry arch bridges. Struct Infr Engng 2016;12(11):1439–64.